AUT Journal of Electrical Engineering

AUT J. Elec. Eng., 55(3) (Special Issue) (2023) 417-440
DOI: 10.22060/eej.2023.22276.5528

Parallel Real-time Nonlinear Model Predictive Control of DFIG-based Wind Turbines over All Operating Regions

M. Soleymani, M. Rahmani*, N. Bigdeli

Department of Electrical Engineering, Imam Khomeini International University, Qazvin, Iran

ABSTRACT: Nonlinear model predictive control (NMPC) is a viable solution for control problems in the industry. In this paper, a real-time NMPC approach is proposed for the control of wind turbine (WT) over operating regions. Using wind speed predictions, the NMPC achieves the right compromise between maximizing power and reducing WT fatigue loads while limiting the generator torque activity and the blade pitch angle and smoothing out the electrical power. The control scheme is tested in a simulation environment with a set of standard high turbulence wind profiles and coherent gusts, utilizing complete aeroelastic modeling of the WT and an all-nonlinear model of the doubly fed induction generator (DFIG) over the whole operation region. Besides, the NMPC has been implemented in a parallel Newton-type approach to make it more efficient and implementable. A wide range of simulation scenarios, as well as statistical analysis, were also performed to demonstrate the performance and robustness of the proposed controller against model parameter uncertainties. In addition, finite-time convergence of the controller is guaranteed by employing terminal constraints. The results show 1.7% increase in power extraction, 11% decrease in shaft load, and 12% decrease in tower load while reducing the activity of control inputs and smoothing the generator power.

Review History:

Received: Mar. 15, 2023
Revised: Sep. 02, 2023
Accepted: Nov. 07, 2023
Available Online: Dec. 01, 2023

Keywords:

Wind turbine control
real-time NMPC
Load reduction
DFIG
FAST

1- Introduction

As a result of energy shortages and environmental protection requirements, renewable energy, particularly wind energy, has gained global attention nowadays. For cost-effective wind power extraction, Variable Speed WTs (VSWT) with DFIG are usually used [1]. This is because variable-speed operation reduces structural loads while increasing energy capture. DFIGs also offer essential advantages such as separate active and reactive power control and less mechanical pressure on the turbine. However, sophisticated control algorithms are required for VSWTs to be lucrative and reliable [2].

An appropriate VSWT control system helps optimize power generation, improve power quality, and reduce mechanical and aerodynamic stresses on turbine components, resulting in increased installation life. VSWTs operate in two different modes: partial-load and full-load. In partial-load mode, one usual control goal is to regulate the generator speed to extract as much energy from the wind as feasible, while the generator torque gives the control input to change the generator speed. The key objective in the full-load region is to keep the rated power output constant. This is generally managed by having a constant generator torque while varying the pitch angle. The turbine's response to transient loads must be reduced in both operating regions [3].

A high-performance VSWT control approach has become a difficult challenge because the VSWT system has a nonlinear multi-variable, multi-constraint, and strongly coupled non-affine structure in addition to the stochastic aspect of the wind input [4]. On the other hand, with the size of WTs continually rising, interest in using advanced controllers to reduce structural fatigue is growing, particularly in towers and drivetrains. Tower failure, mainly due to its fore-aft oscillations, can lead to the destruction of the plant [5, 6]. In addition, gearbox-related failures are responsible for more than 20% of the downtime of WTs [7]. However, a multi-variable nonlinear controller that adjusts both the generator torque and the blade pitch can reduce these effects to some extent. This controller is supposed to use wind speed information before colliding with the turbine in its design. In that case, it can react in time and make a good compromise between power generation and load reduction [8]. Wind disturbances may be predicted using light detection and ranging (LIDAR) systems at different distances in front of WTs. This technique opens the door to developing wind energy control concepts such as model predictive control (MPC) and feedforward control [9].

Many control methods have been developed to control WTs at low and high wind speeds [8]. A significant review of this literature has been conducted in [10-13]. Classical controllers such as PI/PID controllers [14], LQ/LQG-based controllers [15], and linear controllers [16] are widely used for this purpose. However, linear controllers

*Corresponding author's email: mrahmani@eng.ikiu.ac.ir

Copyrights for this article are retained by the author(s) with publishing rights granted to Amirkabir University Press. The content of this article is subject to the terms and conditions of the Creative Commons Attribution 4.0 International (CC-BY-NC 4.0) License. For more information, please visit https://www.creativecommons.org/licenses/by-nc/4.0/legalcode.

in WTs typically result in poor dynamic performance and the inability to systematically incorporate system and input constraints. Adaptive linear regulators [17, 18] and gain-scheduling controllers [19] are developed to deal with system nonlinearity. Advanced control methods use fault-tolerant control [20, 21], sliding mode control [22-24], and MPC [25] as well. However, many of the papers concentrate on designing the control system in either the full load or partial load region. One of the motivations for writing this paper was the scarcity of studies on developing an overall MIMO control strategy that can work in both regions.

The ability to handle complicated WT operational limitations, model nonlinearities, elaborate operational strategies, the introduction of additional actuators, and the growing LIDAR sensors are the key motivations for adopting advanced control approaches for wind turbine control (WTC). In simulations, promising results have been achieved, indicating that linear MPC [26-28], adaptive MPC [29], and NMPC [25, 30, 31] methods have the potential to outperform more classic control approaches. A review of MPC applications for WT is presented in [32] and [33]. Most publications, however, focus on aero-turbine control [34] or generator control [35] and are designed for a particular operational area.

Higher computational costs prevent NMPCs from using more accurate models and complex control schemes and prevent their more comprehensive real-time application. Fortunately, with the rapid development of parallel devices such as Field-Programmable Gate Arrays (FPGAs), graphics processing units, and multi-core processors, parallel real-time algorithms for solving Optimal Control Problems (OCPs) have been developed [36, 37]. Using these parallel algorithms can significantly reduce the computational time of NMPCs [38]. In [31], an NMPC controller is evaluated across the whole operation area using a realistic aeroelastic model of the WT, but real-time calculations aren't discussed. The reference [39] describes a real-time NMPC technique for WT but does not investigate detailed fatigue load analysis. Moreover, the controller is not examined when the model is uncertain and complete and accurate wind information is not available.

In this paper, a constrained parallel real-time NMPC controller is designed and analyzed for control of WT over its all-operating regions. Using wind speed predictions, the NMPC achieves the right compromise between maximizing power and reducing WT fatigue loads while limiting the generator torque activity and the blade pitch angle and smoothing out the electrical power. The NMPC has been implemented in a parallel Newton-type approach to make it more efficient and implementable as well. The control scheme is tested in a simulation environment using a set of high-turbulence wind profiles, coherent gusts, and a precise aeroelastic model of the WT across the whole operation area. Because of the parallelism of the NMPC controller's optimization technique, the computational time is considerably decreased despite the complexity of the controller. Furthermore, for all simulations, the stability of the NMPC in the sense of convergence is ensured using terminal elements. The controller is also evaluated when the model is uncertain and complete and accurate wind data is unavailable. In general, the main features and contributions of this article are as follows:

(1) A constrained multivariable NMPC controller is presented to control DFIG-based VSWT in all the operating regions.

(2) The designed NMPC has been solved using a parallel Newton-type method [38], making it more efficient and implementable.

(3) For all simulations, the stability of the NMPC in the sense of convergence is ensured using terminal elements.

(4) The MLife tool performs fatigue estimates and provides statistical information for WT [40]. The controller is evaluated in scenarios when the model is uncertain and complete and accurate wind information is unavailable.

(5) For both the aero-turbine and the DFIG models, a nonlinear model is used, and unlike most articles, no simplification assumptions are considered for the DFIG model. This brings the model closer to the real-world physical model.

(6) FAST (fatigue, aerodynamics, structures, and turbulence) [41] is used for the exact aeroelastic model. It is disturbed by TurbSim's standard wind fields [42]. This makes the simulations more realistic.

The following is how this article is organized: Section 2 presents the aero-turbine and DFIG models. The VSWT control techniques and goals are then thoroughly detailed. The proposed controller design is covered in Section 3. Section 4 shows simulation results using the complete aeroelastic model perturbed by stochastic wind profiles and coherent gusts. At the end of this section, the simulations are repeated when the model has uncertainty and complete and accurate wind information is not available. Section 5 is a summary of our findings. The WT and DFIG parameters are presented in the appendix.

2- Wind turbine modeling

A 5 MW horizontal axis VSWT is considered in this work. Fig. 1 depicts a typical VSWT structure [43]. Definitions of variables and parameter values are presented in the nomenclature table and Appendix A.

2- 1- Aero-turbine model

Modeling a controlled plant plays a crucial role in designing an appropriate predictive controller. The model must be accurate enough to model the critical dynamics of the WT yet simple enough to accept the predictive controller's computational time. This study uses an exact aeroelastic model to validate the results. However, this model is too complex to be used in MPC. Thus, a reduced model forms the internal model of the MPC.

2- 1- 1- Aeroelastic model

The governing equations of a WT are highly nonlinear. Therefore, a variety of simulators for designing and modeling

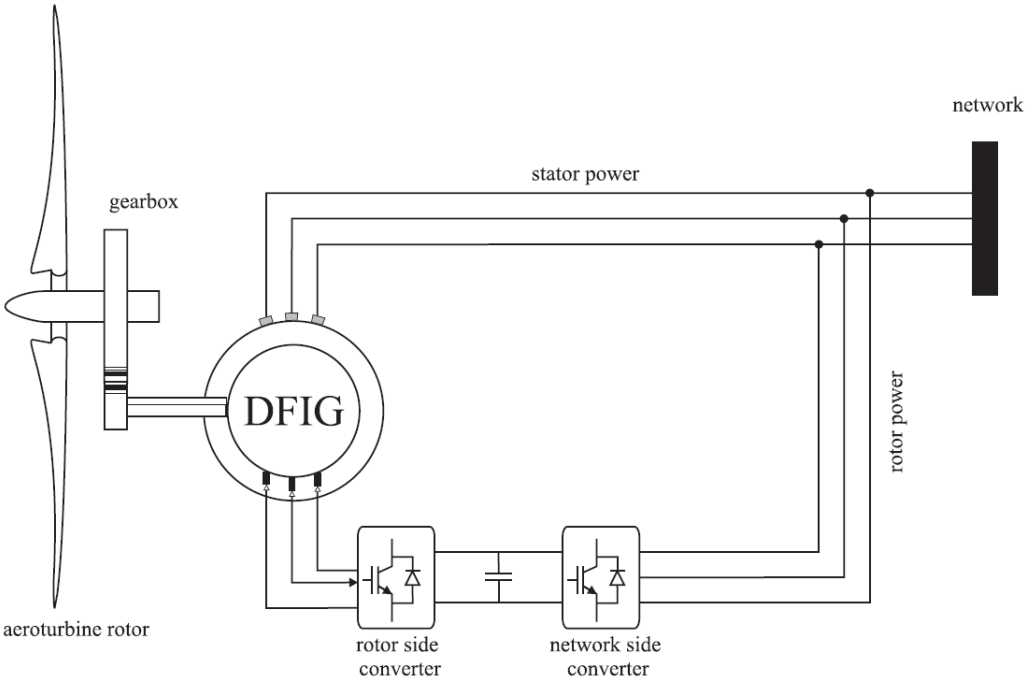

Fig. 1. Common configuration for variable speed wind turbine.

WTs are presented in [44-47]. Simulations of a 5-MW three-bladed VSWT designed by the National Renewable Energy Laboratory (NREL) are done here using an aeroelastic code, as described in [41]. WT designers use this code to estimate both extreme and fatigue loads. Drivetrain rotational flexibility, first and second fore-aft, and side-to-side tower bending modes, first and second flapwise and first edgewise blade modes, yaw, and generator are among the 16 degrees of freedom enabled in the FAST simulation. Appendix A shows the parameters of this WT.

2- 1- 2- Reduced nonlinear model

This section introduces a simplified model of the aeroelastic model described in Section 2.1.1. Fig. 2 shows a schematic of this model. The WT first captures the wind's kinetic energy mechanically, then transmits it through the drivetrain shaft. The generator converts it into electrical energy and delivers it to the grid. Eqs. (1) show the nonlinear dynamics of the reduced model of the WT in the state space form [48-50]:

$$\dot{X} = f(X,U,v_0) = \begin{bmatrix} \omega_r - \omega_g / n_g \\ 1/J_r(T_a(\omega_r,\dot{x}_T,\beta,v_0) - T_{ls}(\theta_s,\omega_r,\omega_g) - K_r\omega_r) \\ 1/J_g(T_{hs}(\theta_s,\omega_r,\omega_g) - K_g\omega_g - T_{em}) \\ \dot{x}_T \\ 1/m_{Te}(F_a(\omega_r,\dot{x}_T,\beta,v_0) - c_T\dot{x}_T - K_T x_T) \\ \dot{T}_{em} \\ \dot{\beta} \end{bmatrix} \quad (1)$$

$$T_a = \frac{1}{2}\rho_{air}\pi R^3 C_q(\lambda,\beta)v^2,$$

$$F_a = \frac{1}{2}\rho_{air}\pi R^2 C_t(\lambda,\beta)v^2,$$

$$T_{ls} = B_{ls}\theta_s + K_{ls}(\omega_r - \frac{\omega_g}{n_g}), T_{hs} = \frac{T_{ls}}{n_g}$$

$$\lambda = R\times\frac{\omega_r}{v}, v = v_0 - \dot{x}_T, C_q(\lambda,\beta) = \frac{C_p(\lambda,\beta)}{\lambda}$$

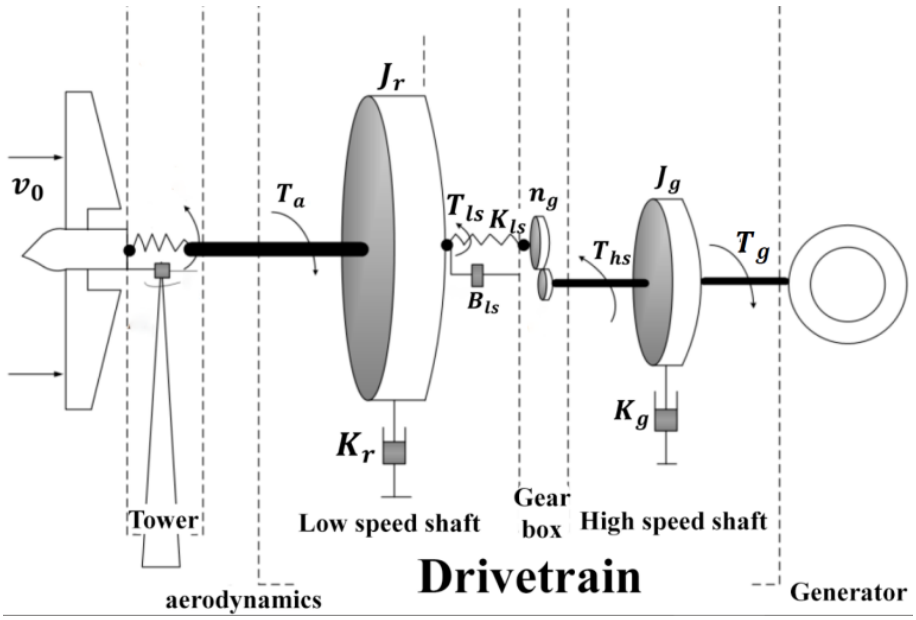

Fig. 2. The mechanical structure of the VSWT.

We define the state and input of WTs with $X=\left[\theta_s,\omega_r,\omega_g,x_T,\dot{x}_T,T_g,\beta\right]^T$, and $U=\left[\dot{T}_{em},\dot{\beta}\right]^T$, respectively. The variable ω_r represents the rotor speed, and J_r and K_r are its inertia and external damping, respectively. Also, the variable ω_g represents the generator speed, and J_g and K_g are its inertia and external damping. x_T is the fore-aft displacement of the nacelle caused by tower oscillations. v_0 is the natural wind speed, and v is its apparent speed due to the tower displacements. T_{ls} and T_{hs} show low-speed and high-speed shaft torque, respectively. Parameters K_{ls} and B_{ls} show the damping and stiffness of the low-speed shaft, respectively. T_a and F_a are variables that represent aerodynamic torque and thrust, respectively. θ_s shows the shaft torsion. T_{em} is the electromagnetic torque, and n_g is the gear ratio. Parameters R and ρ_{air} represent the rotor radius and the air density, respectively.

The power, torque, and thrust coefficients are represented by the variables C_q, C_p, and C_t. These coefficients are nonlinear functions of the Tip Speed Ratio (TSR), λ, and the pitch angle, β. We consider the coefficients $C_p(\lambda,\beta)$ and $C_t(\lambda,\beta)$ in the model as fitting polynomials to their related lookup tables (see Fig. 3), which may be achieved through steady-state simulations, e.g., created using the FAST code [41].

The values of the tower's equivalent modal mass, m_{T_e}, structural damping, c_T, and bending stiffness, k_T, were computed using [31] and are shown in Appendix A:

$$\begin{aligned} m_{Te} &= 0.25m_T + m_N + m_H + 3m_B \\ C_T &= 4\pi m_{Te} d_s f_0 \\ k_T &= m_{Te}(2\pi f_0)^2 \end{aligned} \tag{2}$$

The fore-aft bending moment at the base of the tower, M_{yT}, is determined by

$$m_{yT} = h_H(c_T\dot{x}_T + k_T x_T) \tag{3}$$

2- 2- Generator model

Most articles use the DFIG model because it is a common and efficient model [51, 52]. A rotating (d,q) frame is considered for modeling the DFIG. This rotating frame is linked to the stator flux vector, and its *d*-axis coincides with the stator flux vector. Therefore, the components of the stator flux vector are expressed as:

$$\phi_{sd} = \phi_s, \phi_{sq} = 0 \tag{4}$$

DFIG dynamics can be described in the (d,q) frame by the following differential equations [53]:

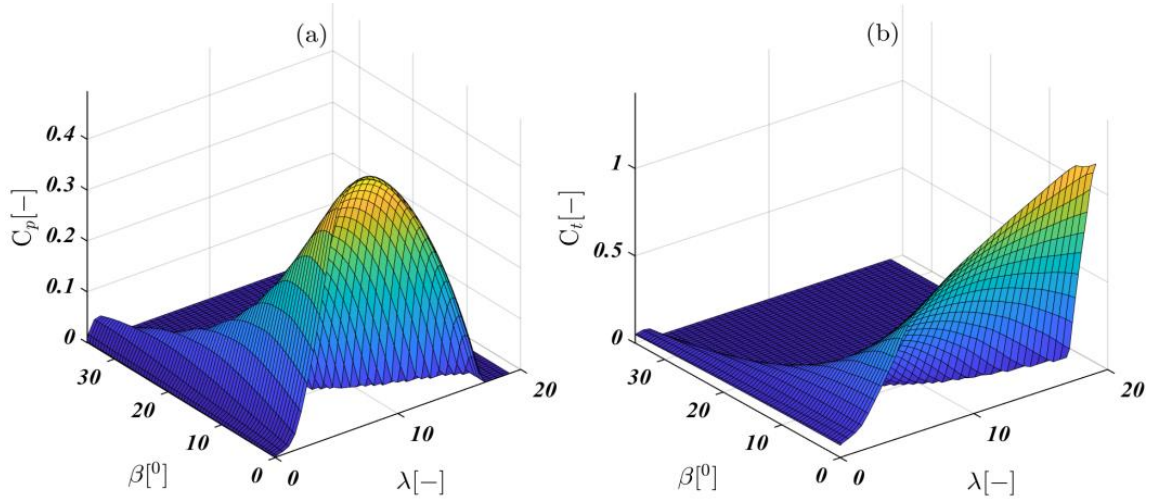

Fig. 3. (a) Effective power coefficient curve. (b) Effective thrust coefficient curve.

$$\frac{d\phi_{sd}}{dt} = -\alpha\phi_{sd} + M\alpha i_{rd} + v_{sd}$$

$$\frac{d\rho}{dt} = \frac{M\alpha i_{rq} + v_{sq}}{\phi_{sd}}$$

$$\frac{di_{rd}}{dt} = \alpha\beta\phi_{sd} - \gamma i_{rd} + \frac{M\alpha i_{rq}^2}{\phi_{sd}} + \frac{i_{rq}v_{sq}}{\phi_{sd}} - P\omega_g i_{rq} - \beta v_{sq} + \frac{1}{\sigma}v_{rd}$$

$$\frac{di_{rq}}{dt} = \beta P\omega_g\phi_{sd} - \frac{M\alpha i_{rd}i_{rq}}{\phi_{sd}} - \frac{i_{rd}v_{sq}}{\phi_{sd}} - P\omega_g i_{rd} - \gamma i_{rq} - \beta v_{sq} + \frac{1}{\sigma}v_{rq} \quad (5)$$

with

$$\sigma = L_r(1-\frac{M^2}{L_r L_s}), \alpha = \frac{R_s}{L_s},$$

$$\beta = \frac{M}{\sigma L_s}, \lambda = \frac{R_r}{\sigma} + \beta\alpha M .$$

Because the DFIG is driven by the rotor-side converter, just the rotor voltages v_{rd} and v_{rq} are considered control inputs. Appendix A contains the DFIG parameters. The aero-turbine model and the generator model are connected by electromagnetic torque, which is described by the following description:

$$T_{em} = -P\frac{M}{L_s}\phi_s i_{rq} \quad (6)$$

2- 3- Wind turbine control schemes and their corresponding objectives

In the classical WTC approach, the control objectives determine the WT operating regions in terms of wind speed. These objectives usually maximize power generation, P_g , and maintain the stress on the WT structure and actuators at a reasonable level. In Fig. 4, we show the values of electromagnetic torque, T_{em} , generator speed, ω_g , pitch angle, β , and tower top fore-aft displacement, x_T , in a steady state for the classical control approach in terms of wind speed. We use these steady-states in the proposed controller. In Region 1, the wind speed causes the WT to start. Power extraction is not economical since the wind speed is lower than the cut-in wind speed (V_{cut-in}). Therefore, the generator's torque input is zero. In region 2 (the partial load region), the power is maximized by maximizing the power coefficient $C_p(\lambda,\beta)$, i.e.,

$$\lambda^*, \beta^* = \max_{\lambda,\beta} C_p(\lambda,\beta) \quad (7)$$

The optimal steady-state rotor speed is also calculated as

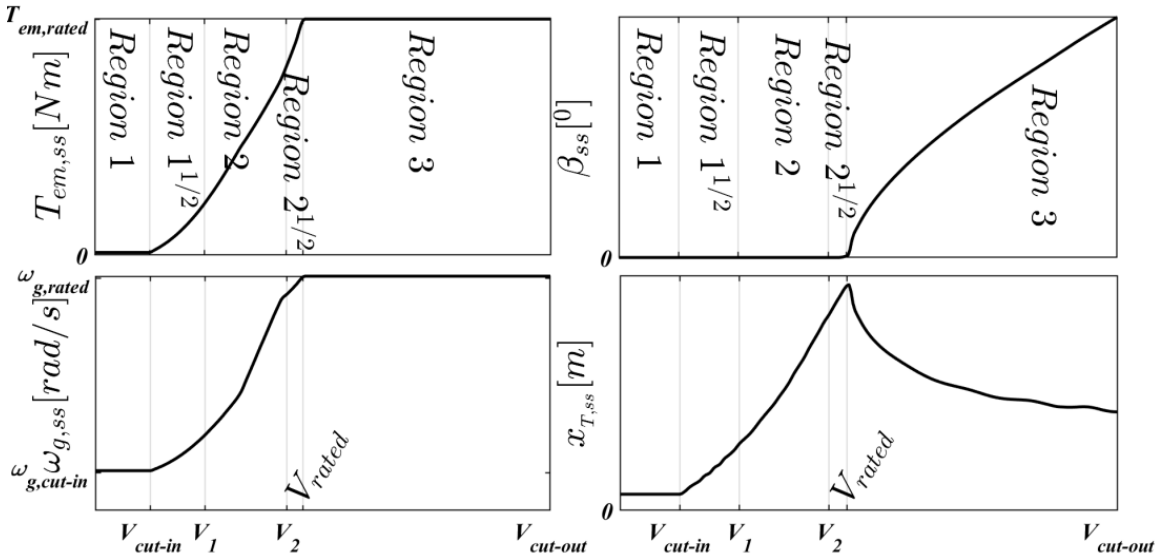

Fig. 4. Operating points corresponding to a common control strategy [41].

follows:

$$\omega_r^*(v_0)=\frac{\lambda^* v_0}{R} \tag{8}$$

The generator torque is proportional to the square of the generator speed, and the blade pitch angle is zero. In region 3 (full load region), the generator speed, torque, and power reach their rated values. The pitch angle β is changed so that the value of the power coefficient $C_p(\lambda,\beta)$ decreases and the generator speed remains at its rated value (see [41, 54, 55] for more details).

In addition to the above control objectives, the following conditions must be satisfied in the development of a successful VSWT control system:

- Minimizing transient loads on the drivetrain. Increasing mechanical vibrations in the drivetrain may lead to fatigue damage.
- Structural fatigue reduction. Tower fore-aft oscillations are the primary focus of structural fatigue management.
- Minimizing the pitch control activity and generator torque control activity.
- Oscillations in the electrical power delivered to the grid can shorten the life of turbine components and cause voltage flicker problems.
- Due to safety and operational concerns, constraints must be observed in a WT.

3- The proposed controller design

A multivariable NMPC is designed in this section. This controller combines two cascaded controllers: an NMPC aero-turbine controller in the outer loop and a DFIG controller in the inner loop. The schematic of this controller is shown in Fig. 5. The external control loop is the predictive aero-turbine controller, while the internal control loop is the DFIG controller. The outer loop, which is the proposed controller, is designed in this section. For the inner loop, we consider the all-nonlinear DFIG model (5) and control it using the existing nonlinear state feedback controller [25]. The external loop gives references $T_{em_{ref}}$ and $\phi_{s_{ref}}$ to the internal loop and produces the pitch angle control signal β for the aero-turbine. The DFIG controller then generates control inputs v_{rd} and v_{rq} in such a way that the tracking error values of stator flux and electromagnetic torque are minimized. Therefore, one can then consider that $T_{em}=T_{em_{ref}}$ and $\phi_s=\phi_{s_{ref}}$ (for more details and how to design a DFIG controller, see [25]).

3- 1- Aero-turbine nonlinear predictive controller

MPC is classified into two types: linear and nonlinear models. On the other hand, many realistic systems feature nonlinearities that must be considered. When nonlinear models, objective functions, and constraints are considered, NMPC usually gives better results. The following are the major advantages of using MPC [33]:

Control tasks that need multivariable and non-quadratic control can be handled easily by the MPC method.

When addressing the OCP, MPC includes actuator and

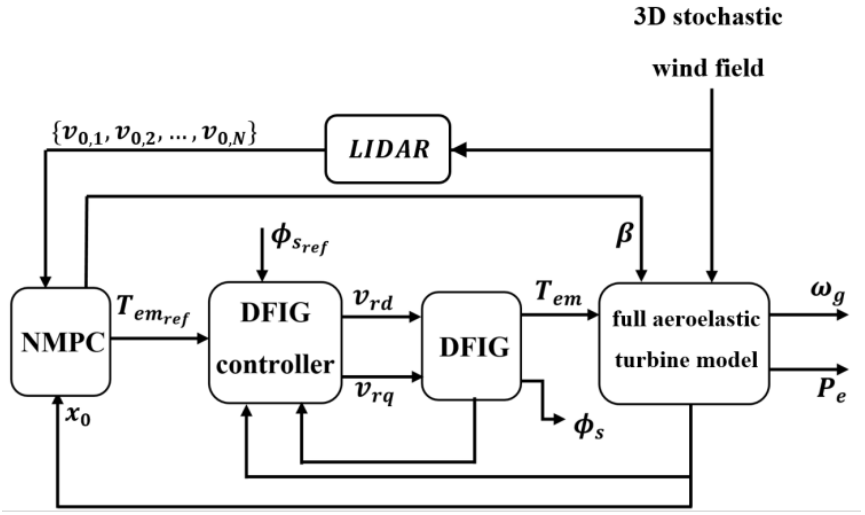

Fig. 5. Multivariable NMPC controller.

system limitations.

On top of all that, it gives a simple way to tune the MPC controller by altering the weight of an objective function, and it allows for the incorporation of a disturbance preview in real-time.

Using an internal model and current measurements, MPC could predict system behavior. Control actions are calculated with this information by using an OCP over a particular time horizon. Once the new measurements are taken, a new solution to the optimal OCP is found based on some of the control input solution trajectories. As the OCP is initialized with the current state of the turbine, feedback is obtained. In this subsection, the OCP is derived for the aero-turbine and solved in real-time (see Algorithm 1).

3- 1- 1- Stage cost function

The NMPC is designed to achieve the objectives mentioned in section 2.3. A quadratic form is assumed for the stage cost function L as follows:

$$L(u,x,v_0) := \frac{1}{2}\left(\left\|x - x_{ref}(v_0)\right\|^2_{Q(v_0)} + \left\|u\right\|^2_{R(v_0)}\right) \quad (9)$$

where vectors x and u form the states and inputs of the wind turbine system, respectively.

$$x = [\theta_s, \omega_r, \omega_g, x_T, \dot{x}_T, T_{em}, \beta]^T, u = [\dot{T}_{em}, \dot{\beta}]^T \quad (10)$$

MPC tracking is based on tracking the reference trajectories that are wind-dependent here. Therefore, the vector $x_{ref}(v_0)$ contains the steady-state values of the system (1) and is defined as follows:

$$\begin{aligned} x_{ref}(v_0) = [&\theta_{s,ss}(v_0), \omega_{r,ss}(v_0), \omega_{g,ss}(v_0), \\ &x_{T,ss}(v_0), \dot{x}_{T,ss}(v_0), T_{em,ss}(v_0), \beta_{ss}(v_0)]^T \end{aligned} \quad (11)$$

These steady-state values may be determined using steady-state simulation, such as FAST, as illustrated in Fig. 4 (see, e.g., [41]). The weighting matrix of the deviation from steady-state Q and the control input weighting matrix R change their values at the rated wind speed:

$$Q(v_0) = \begin{cases} diag(Q_{II,\theta_s}, Q_{II,\omega_r}, Q_{II,\omega_g}, \\ Q_{II,x_T}, Q_{II,\dot{x}_T}, Q_{II,T_{em}}, Q_{II,\beta}), \\ v_0 \le v_{rated} \\ diag(Q_{III,\theta_s}, Q_{III,\omega_r}, Q_{III,\omega_g}, \\ Q_{III,x_T}, Q_{III,\dot{x}_T}, Q_{III,T_{em}}, Q_{III,\beta}), \\ v_0 > v_{rated} \end{cases} \quad (12)$$

$$R(v_0) = \begin{cases} diag(R_{II,\dot{T}_{em}}, R_{II,\dot{\beta}}), v_0 \le v_{rated} \\ diag(R_{III,\dot{T}_{em}}, R_{III,\dot{\beta}}), v_0 > v_{rated} \end{cases} \quad (13)$$

In this paper, two sets of control parameters have been

chosen. The values of these control parameters are given in Table 2. In the first set, $NMPC_1$, these parameters are adjusted so that the best trade-off between power extraction, fatigue loads (the oscillations of shaft torsion θ_s and the oscillations of tower top fore-aft displacement x_T), generator activity, and pitch activity are achieved. For example, since the reduction of fatigue loads is more critical in region 3 than in region 2, the weights Q_{III,θ_s}, Q_{III,x_T}, and $Q_{III,\dot{x}_T}$ take higher values than the weights Q_{II,θ_s}, Q_{II,x_T}, and $Q_{II,\dot{x}_T}$. Because the loads on the shaft will increase significantly if the rotor speed in egion 2 is perfectly tracked, the weights Q_{II,ω_r}, and Q_{II,ω_g} are chosen significantly less than Q_{III,ω_r} and Q_{III,ω_g}. In addition, the weights of $Q_{III,T_{em}}$, $Q_{II,\beta}$, $R_{II,\dot{T}_{em}}$, and $R_{III,\dot{\beta}}$ are picked with greater values than the weights of $Q_{II,T_{em}}$, $Q_{III,\beta}$, $R_{III,\dot{T}_{em}}$, and $R_{II,\dot{\beta}}$, to smooth the generator torque and pitch and reduce the activity of their actuator systems. The compromise in the second set, $NMPC_2$, is done in such a way as to pay more attention to power extraction in region 2 and fatigue load reduction in region 3.

3- 1- 2- System dynamics and operational constraints

The OCP of the WT is subject to the WT's dynamics system and its operational constraints. For the system dynamics, we consider the discrete-time form of Eqs. (1) that discretizes with the Euler method:

$$\begin{bmatrix} \theta_s(k+1) \\ \omega_r(k+1) \\ \\ \\ \omega_g(k+1) \\ \\ x_T(k+1) \\ \dot{x}_T(k+1) \\ \\ \\ T_{em}(k+1) \\ \beta(k+1) \end{bmatrix} = \begin{bmatrix} \theta_s(k)+\Delta\tau\times(\omega_r(k)-\omega_g(k)/n_g) \\ \omega_r(k)+\Delta\tau/J_r(T_a(\omega_r(k),\dot{x}_T(k), \\ \beta(k),v_0(k))-T_{ls}(\theta_s(k),\omega_r(k), \\ \omega_g(k))-K_r\omega_r(k)) \\ \omega_g(k)+\Delta\tau/J_g((T_{hs}(\theta_s(k),\omega_r(k), \\ \omega_g(k))-K_g\omega_g(k)-T_{em}(k)) \\ x_T(k)+\Delta\tau\times\dot{x}_T(k) \\ \dot{x}_T(k)+\Delta\tau/m_{Te}(F_a(\omega_r(k), \\ \dot{x}_T(k),\beta(k),v_0(k)) \\ -c_T\dot{x}_T(k)-K_Tx_T(k)) \\ T_{em}(k)+\Delta\tau\times\dot{T}_{em}(k) \\ \beta(k)+\Delta\tau\times\dot{\beta}(k) \end{bmatrix} \quad (14)$$

where index k denotes discrete time and $\Delta\tau = T/N$ is the discretization step size. Future values of natural wind speed v_0 can be measured with preview information provided by LIDAR sensors [31].

In addition to the dynamics system, physical limits must be met during operation in VSWT due to limitations in the actuator and safety regulations in the control process. Therefore, we consider the following set of constraints:

$$\omega_{r,\min} \le \omega_r(k) \le \omega_{r,\max} \quad (15)$$

$$\omega_{g,\min} \le \omega_g(k) \le \omega_{g,\max}$$
$$0 \le T_{em}(k) \le T_{em,\max}$$
$$0 \le \beta(k) \le \beta_{\max}$$
$$dT_{em,\min} \le \dot{T}_{em}(k) \le dT_{em,\max}$$
$$d\beta_{\min} \le \dot{\beta}(k) \le d\beta_{\max}$$

where the maximum generator torque $T_{em,max}$, generator speed $\omega_{g,max}$, and rotor speed $\omega_{r,max}$, are set somewhat larger than their rated values $T_{em,rated}$, $\omega_{g,rated}$, and $\omega_{r,rated}$ [39, 41].

3- 1- 3- Optimal control problem definition

The proposed infinite-horizon OCP for WTC strategy can be formulated as follows:

$$\min \sum_{k=0}^{\infty} 1/2(\|x(k)-x_{ref}(v_0(k))\|^2_{Q(v_0)} + \|u(k)\|^2_{R(v_0)}) \quad (a)$$

$$s.t$$

$$\begin{aligned} \theta_s(k+1) &= \theta_s(k)+\Delta\tau\times(\omega_r(k)-\omega_g(k)/n_g) \\ \omega_r(k+1) &= \omega_r(k)+\Delta\tau/J_r(T_a(\omega_r(k),\dot{x}_T(k), \\ &\beta(k),v_0(k))-T_{ls}(\theta_s(k),\omega_r(k),\omega_g(k))- \\ &K_r\omega_r(k)) \\ \omega_g(k+1) &= \omega_g(k)+\Delta\tau/J_g((T_{hs}(\theta_s(k), \\ &\omega_r(k),\omega_g(k))-K_g\omega_g(k)-T_{em}(k)) \\ x_T(k+1) &= x_T(k)+\Delta\tau\times\dot{x}_T(k) \\ \dot{x}_T(k+1) &= \dot{x}_T(k)+\Delta\tau/m_{Te}(F_a(\omega_r(k), \\ &\dot{x}_T(k),\beta(k),v_0(k))-c_T\dot{x}_T(k)-K_Tx_T(k)) \\ T_{em}(k+1) &= T_{em}(k)+\Delta\tau\times\dot{T}_{em}(k) \\ \beta(k+1) &= \beta(k)+\Delta\tau\times\dot{\beta}(k) \end{aligned} \quad (b)$$

(16)

$$\theta_s(0)=\theta_{s,0},\omega_r(0)=\omega_{r,0},\omega_g(0)= \omega_{g,0},x_T(0)=x_{T,0},\dot{x}_T(0)= \dot{x}_{T,0},T_{em}(0)=T_{em,0},\beta(0)=\beta_0 \quad (c)$$

$$\begin{aligned} &-\omega_r(k)-\omega_{r,\min}\le 0,\omega_r(k)-\omega_{r,\max}\le 0, \\ &-\omega_g(k)+\omega_{g,\min}\le 0,\omega_g(k)-\omega_{g,\max}\le 0, \\ &-T_{em}(k)\le 0,T_{em}(k)-T_{em,\max}\le 0, \\ &-\beta(k)\le 0,\beta(k)-\beta_{\max}\le 0, \\ &-\dot{T}_{em}(k)+dT_{em,\min}\le 0,\dot{T}_{em}(k)-dT_{em,\max}\le 0, \\ &\dot{\beta}(k)+d\beta_{\min}\le 0,\dot{\beta}(k)-d\beta_{\max}\le \\ &0,k\in\mathbb{N}_0:=\mathbb{N}\cup\{0\} \end{aligned} \quad (d)$$

Algorithm 1 NMPC Algorithm

for each $k = 0,1, \ldots,$ **do**

1. Measure the system's current state $x = x(0)$.
2. To derive the optimal control sequence u_N^*, solve the optimal control problem of (17).
3. During the next sample interval, utilize the feedback law $\mu_N(x) \coloneqq u_N^*(0)$ to control the system using the first element of u_N^*.
4. Set $k \coloneqq k + 1$

end for

Eq. (16a) is the stage cost function, which must be minimized over an infinite horizon. Eq. (16b) is derived from the WT's dynamics system of Eq. (14) with the initial conditions of Eq. (16c). Inequalities in (16d) are also derived from the WT's operational constraints in (15).

3- 1- 4- NMPC controller

NMPC can find an approximate solution for OCP (16) [56]. To do this, we fix the finite horizon $N \in \mathbb{N}$ and solve the OCP (16) at each step of the NMPC algorithm (see Algorithm 1). In addition, if the appropriate terminal elements are used in the NMPC control strategy, it can be shown that NMPC stability in terms of convergence is guaranteed [57, 58]. Therefore, we consider the compact form of OCP (16) and present the NMPC control strategy with the following terminal elements:

$$\begin{aligned}
&\min \sum_{k=0}^{\infty} 1/2(\left\|x(k)-x_{ref}(v_0(k))\right\|_{Q(v_0)}^2 + \\
&\left\|u(k)\right\|_{R(v_0)}^2 + V_f(x(N))) \\
&s.t \\
&x(k+1) = f(x(k), u(k), v_0(k)) \\
&x(0) = x_0 \\
&G(x(k), u(k)) \le 0, k \in \mathbb{N}_0 \\
&x(N) \in X_f
\end{aligned} \tag{17}$$

where we define the terminal elements, $V_f(x(N))$ and X_f, as follows:

$$\begin{aligned}
&V_f(x(N)) \equiv 0 \\
&X_f = \left\{x \mid x(k) - x_{ref}(v_0(k)) = 0\right\}.
\end{aligned} \tag{18}$$

The OCP of (17) can be solved in real-time using the parallel Newton-type method (see Section 3.1.1.5). The solution to (17) is the optimal trajectories for the state x^* and the input u^*. Finally, the resulting closed-loop system is given by

$$x(k+1) = f(x(k), u(k), v_0(k)), u(k) = u^*(0) \tag{19}$$

3- 1- 5- Real-time solution of optimal control problem

Because the model dynamics of Eq. (14) are nonlinear and a prediction horizon T of several seconds must be considered, the OCP of (17) (the second step of Algorithm 1) must be solved using simultaneous techniques [56]. On the other hand, finding a real-time solution to optimization problems is not an easy task. However, due to the increasing use of parallel devices, parallel NMPC approaches are becoming increasingly necessary. Therefore, in this work, we use a parallel Newton-type method [38] to solve the proposed ENMPC problem (17). The reverse-time integration technique is used in this approach to discretize the original optimization problem on the finite horizon interval $[t, t+T]$ with a discretization step size of $\Delta\tau = T/N$. Then, the resulting Euler-Lagrange equations (often referred to as the Karush-Kuhn-Tucker (KKT) conditions) are linearly coupled between neighboring stages. After that, the KKT conditions are approximately decoupled into single-step subproblems. Finally, it is proved that the convergence rate of the parallel Newton-type method is super-linear under mild conditions; see [38] for more details.

4- Simulation results

In this section, simulations are performed to measure fatigue and extreme loads in two separate subsections for the multivariable NMPC controller described in Section 3. In these simulations, the exact aeroelastic model described in Section 2.1.1 is used to simulate WT, and it is assumed that complete and accurate wind speed information is provided by LIDAR to the NMPC. It is also assumed that the internal model of the NMPC has no uncertainty. In the final subsection, we repeat the simulations for cases where complete and accurate wind speed information is not provided to the NMPC and when the model has uncertainties.

In all simulations, we assume that all states are measurable and provide the complete state vector x_0 to the NMPC through the exact aeroelastic model. We also chose a discretization step size of $\Delta\tau = 0.1s$ and are running real-time simulations on an i7 2.66 GHz/64-bit processor.

For comparison, a PI and baseline controllers are provided [41], which control the WT just by feedback and ignore wind

Table 1. TurbSim wind field specifications.

IEC turbulence characteristic	B
Random speeds per mean wind	6
Mean wind speed at hub height	$4, 6, 8, 10, 12, 14, 16, 18, 20, 22, 24\ m/s$
Vertical grid points	31
Horizontal grid points	31
Time step	$0.1\ s$
Grid height	$145\ m$
Grid width	$145\ m$

Table 2. Control parameters.

Description	Parameter	$NMPC_1$	$NMPC_2$
Prediction horizon	T	$21.6\ s$	$21.6\ s$
Discretization step size	$\Delta\tau$	$0.1\ s$	$0.1\ s$
Weight for shaft torsion	$Q_{II,\theta_s}, Q_{III,\theta_s}$	$1\times10^2, 5\times10^4$	$1\times10^2, 5\times10^4$
Weight for rotor speed	$Q_{II,\omega_r}, Q_{III,\omega_r}$	4,40	25,250
Weight for generator speed	$Q_{II,\omega_g}, Q_{III,\omega_g}$	$4\times10^{-5}, 4\times10^{-4}$	$2.5\times10^{-4}, 2.5\times10^{-3}$
Weight for tower top fore–aft displacement	Q_{II,x_T}, Q_{III,x_T}	1,5	10,50
Weight for tower top fore–aft velocity	$Q_{II,\dot{x}_T}, Q_{III,\dot{x}_T}$	1,5	10,50
Weight for electromagnetic torque	$Q_{II,T_{em}}, Q_{III,T_{em}}$	$0{,}1\times10^{-7}$	$0{,}2\times10^{-7}$
Weight for pitch angle	$Q_{II,\beta}, Q_{III,\beta}$	$5\times10^{-3}, 0$	$5\times10^{-3}, 0$
Weight for electromagnetic torque rate	$R_{II,\dot{T_{em}}}, R_{III,\dot{T_{em}}}$	$2.5\times10^{-8}, 1\times10^{-8}$	$5\times10^{-9}, 1\times10^{-8}$
Weight for pitch angle rate	$R_{II,\dot{\beta}}, R_{III,\dot{\beta}}$	$2.5\times10^{-2}, 2.5$	$2.5\times10^{-2}, 2.5\times10^{-2}$

information. These controllers consist of two parts: one for variable-speed generator torque and another for collective pitch control (CPC). The coefficients of the PI controller for the generator torque and pitch angle are set as follows (see [41] for more details):

$$k_{P,T_{em}} = 97.37, k_{I,T_{em}} = 12.69, k_{P,\beta} = 7.27\times10^{-3}, k_{I,\beta} = 3.11\times10^{-3}$$

4- 1- Fatigue loads

For an accurate analysis of fatigue loads, 11 wind speed bins (of a width of $2\,m/s$ from $v_{cut-in} = 3m/s$ to $v_{cut-out} = 25$) are considered, then for each bin, 6 wind speed profiles are generated with different random seeds by TurbSim and a total of 66 10-minute simulations are performed for the proposed controller. Using TurbSim wind fields (see Table 1), which have B-type turbulence intensity and a Rayleigh distribution with $C = 2m/s$ as defined by IEC 61400-1, the exact aeroelastic model is disturbed [42]. Two sets of control parameters are presented in Table 2 (see Section 3.1.1.1). The NMPC controller stabilizes the closed-loop responses and increases the controller's performance. The following two subsections include instances of these simulations for partial and full load operating areas, and in the following subsection, the computational times of the NMPC are investigated. In the final subsection, general evaluation and stochastic analysis are performed.

4- 1- 1- Simulation in the partial load region

Fig. 6 shows the results of one of 66 simulations (mean wind speeds of $8m/s$ and the random seed of 6) to analyze the performance of the controllers in the partial load region. In this simulation, the maximum of T_{em} and

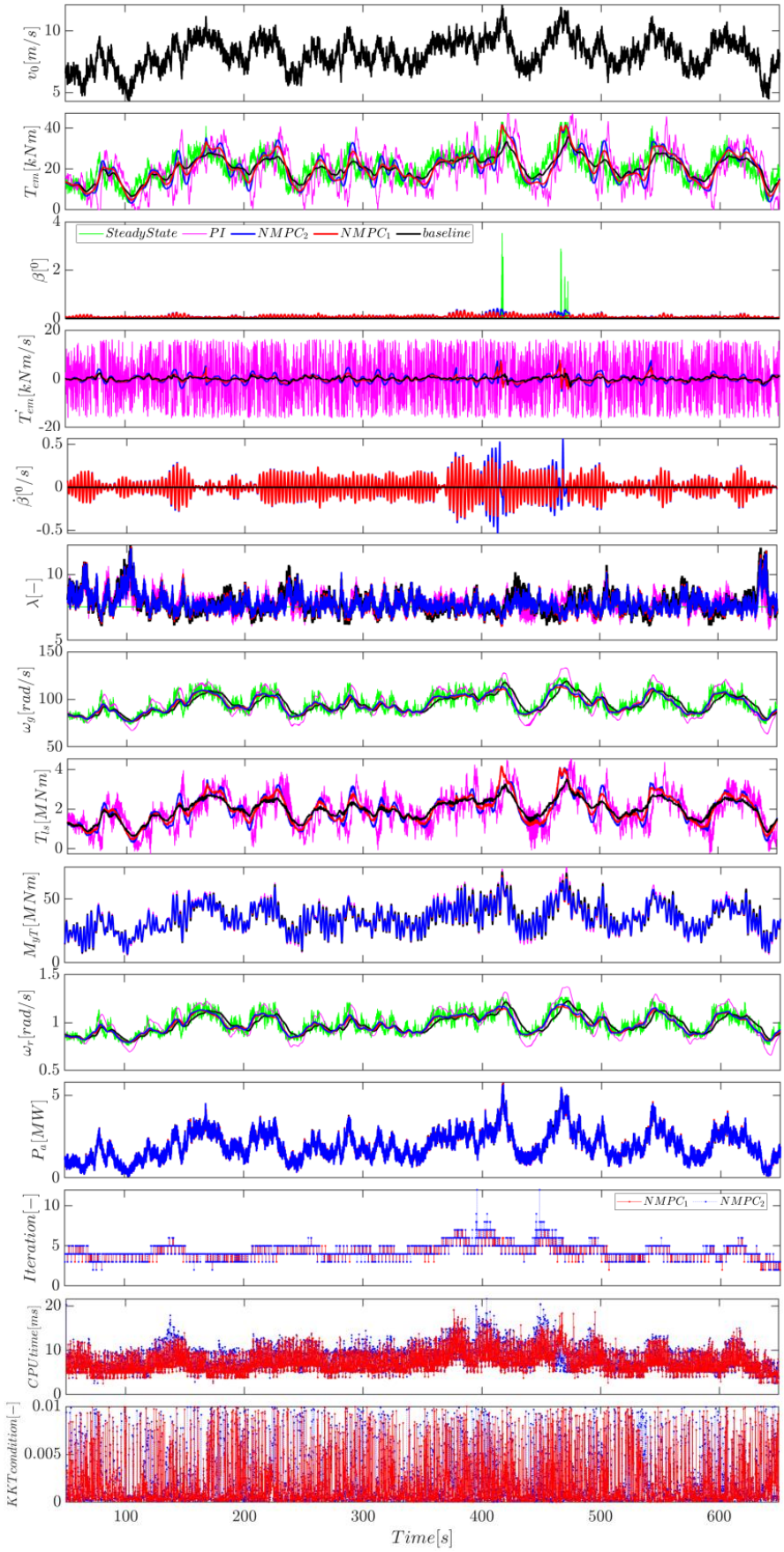

Fig. 6. Simulation results for partial load region (mean wind speeds of 8 m/s and random seed of 6).

Table 3. Comparison of power capture optimization between predictive and conventional controllers.

	$NMPC_1$	$NPMC_2$	baseline	PI
$\eta_{aero}(\%)$	98.36	98.82	97.78	83.49
$\eta_{elec}(\%)$	93.13	93.14	93.13	78.31

T_{ls} in the $NMPC_1$ and $NMPC_2$ controllers are higher than the baseline controller, but they track the optimal TSR λ_{opt} more accurately. With its smooth electromagnetic torque activity, $\dot{T}_{em}$, the $NMPC_1$ controller has a more accurate tracking generator speed ω_g than the baseline controller while maintaining smooth tracking. Therefore, $NMPC_1$ can extract more wind power than the baseline controller (See Table 3 and Table 5). This increases the shaft loads slightly in the partial load area. the $NMPC_2$ has even more accurate generator speed tracking than the $NMPC_1$, which results in more power extraction. This, however, is accompanied by a significant increase in the activity of electromagnetic torque T_{em} and shaft loads in the partial load region. In the baseline controller for the partial load region, the value of β is fixed at the optimum value of 0^0. However, in the NMPC, the value of β to maximize power and reduce the mechanical load remains close to 0^0. Hence, the tower base oscillations M_{yT} in the NMPC controller are reduced (Also see Fig. 9). As expected, the PI controller performs weaker than other controllers in power extraction and load reduction.

Power capture optimization is compared using two criteria: the aerodynamic η_{aero} and the electrical η_{elec} efficiency. They are defined as follows [48]:

$$\eta_{aero}(\%)=\frac{\int_{t_{ini}}^{t_{fin}} P_a dt}{\int_{t_{ini}}^{t_{fin}} P_{a_{opt}} dt}, \eta_{elec}(\%)=\frac{\int_{t_{ini}}^{t_{fin}} P_g dt}{\int_{t_{ini}}^{t_{fin}} P_{a_{opt}} dt} \quad (20)$$

where $P_{a_{opt}}=1/2\rho\pi R^2 C_{p_{opt}} v^3$ denotes the optimal aerodynamic power related to the wind speed profile. These criteria are given in Table 3 for the results in Fig. 6.

The aerodynamic efficiency, η_{aero}, of the baseline controller is 0.58% lower than that of the $NMPC_1$ and 1.04% lower than that of the $NMPC_2$. The electrical efficiencies, η_{elec}, of NMPCs and baseline controllers, are almost equal, while the PI controller is 14.82% lower than them.

4- 1- 2- Simulation in the full-load region

Fig. 7 shows the results of another set of 66 simulations (mean wind speeds of $16 m/s$ and the random seed of 2) to analyze the performance of the controllers in the full load region. As shown in the figure, when compared to the baseline controller, the predictive behavior of $NMPC_1$ can minimize ω_g, P_g, T_{ls}, and M_{y_T} variations with smoother $T_{.em}$ and β, and thus with less pitch and generator activity ($\dot{\beta}$ and $\dot{T}_{em}$), respectively. As a result of these improvements, power extraction at the full load region is enhanced (see Table 5) and the WT useful life is extended. The $NMPC_2$ the controller can further improve the above performances compared to the $NMPC_1$ controller by accepting the cost of increasing the blade pitch activity (see also Fig. 9 and Table 5). The PI controller performs much weaker than NMPCs in power regulation and load reduction.

4- 1- 3- Computational information of optimization algorithm

The degrees of parallelism (DOP) of the Newton-type NMPC optimization method are taken to be 2, 4, and 6 in every third of the 66 simulations, enabling them to be run in parallel on cores 2, 4, and 6, respectively. Figs. 6 and 7 illustrate the computational information of this algorithm, such as the number of iterations, computational time, and KKT condition, for two instances of 66 simulations with DOP = 6 and DOP = 2. The overall computational time is much less than the discretization step size $\Delta\tau=0.1s$, making a real-time implementation straightforward. Fig. 8 shows the maximum, mean, and standard deviation of the optimization algorithm's computational information for DOPs 2, 4, and 6 in all wind bins.

Table 4 depicts the maximum, mean, and standard deviation of the optimization algorithm's computational times for DOPs 2, 4, and 6 under different prediction horizons. As seen in the table, $NMPC_2$ has a shorter computational time than $NMPC_1$ due to the higher activity of $NMPC_2$ control inputs than $NMPC_1$. It should be noted that the maximum computational times are conservative and are only used as a guideline because the simulations were not run on a real-time system. However, they are less than the discretization step size $\Delta\tau=0.1s$.

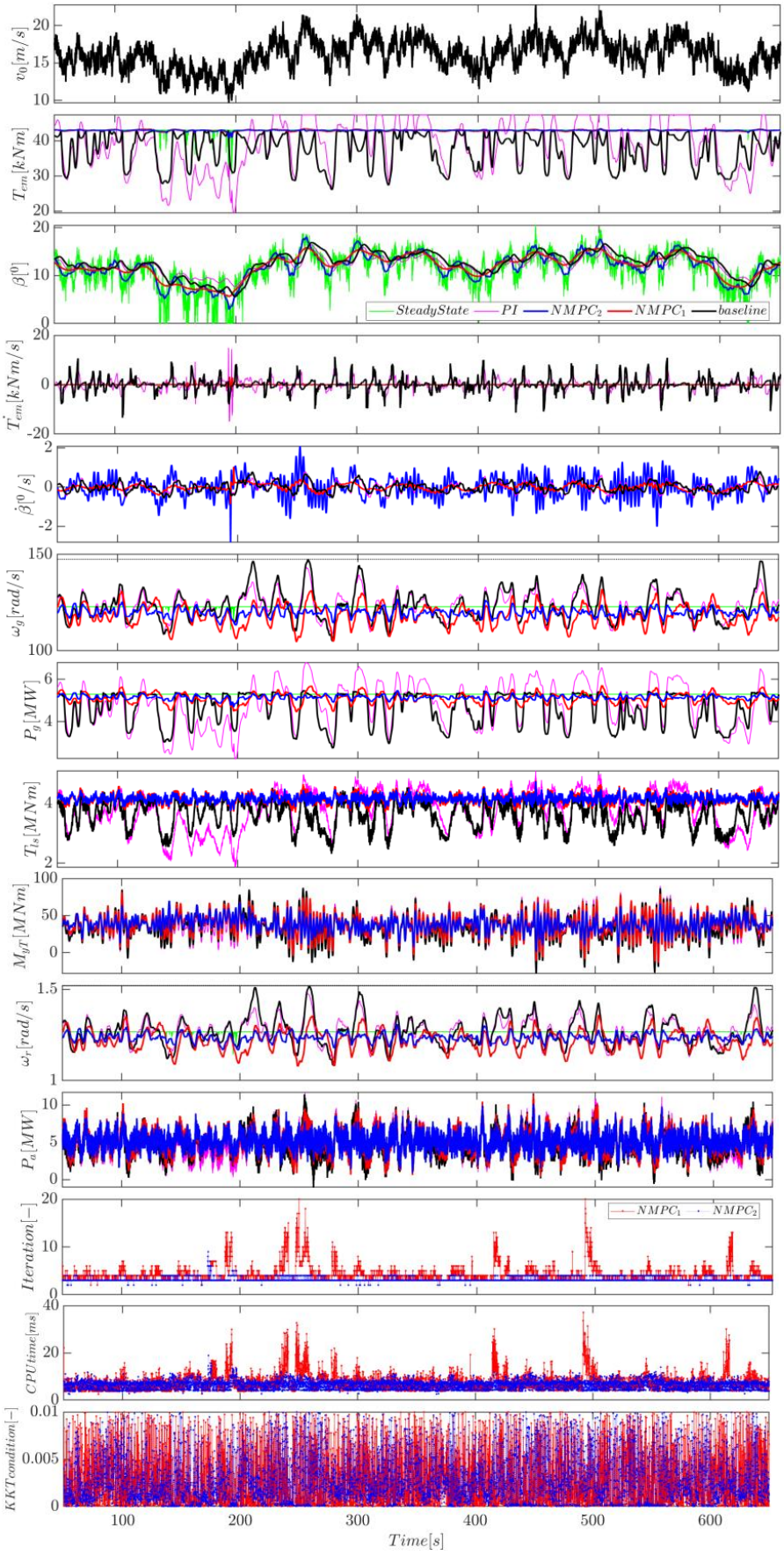

Fig. 7. Simulation results for full load region (mean wind speeds of 16 m/s and random seed of 2).

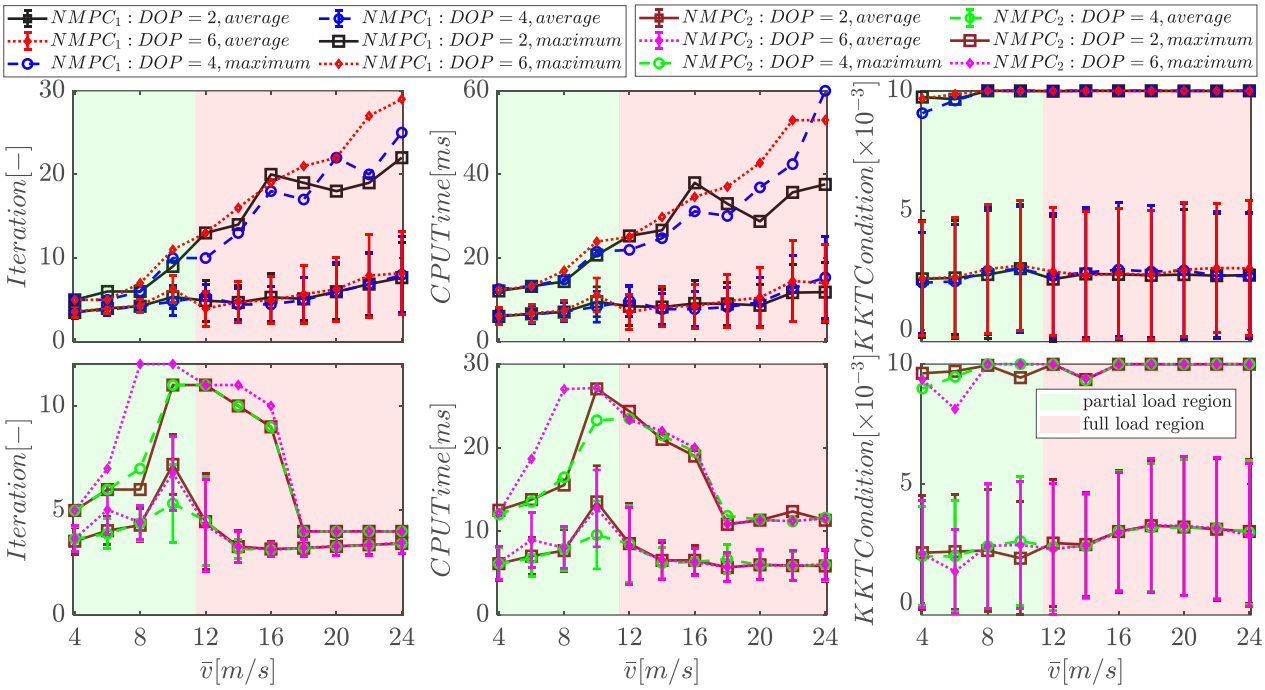

Fig. 8. Optimization algorithm's computational information for DOPs 2, 4, and 6 in all wind bins.

Table 4. Optimization algorithm's CPU time for DOPs 2, 4, and 6 under different prediction horizon.

Prediction Horizon		**21.6 *s***			**16.8 *s***			**12 *s***			**7.2 *s***			**3.6 *s***		
DOP		**2**	**4**	**6**	**2**	**4**	**6**	**2**	**4**	**6**	**2**	**4**	**6**	**2**	**4**	**6**
mean (ms)	$\boldsymbol{NMPC_1}$	8.5	8.9	9.2	**6.7**	6.9	7.6	4.5	4.9	5.2	2.2	2.4	2.6	1.4	1.6	1.8
	$\boldsymbol{NMPC_2}$	**6.9**	**6.7**	**7.1**	6.97	**5.4**	**5.9**	**3.7**	**4.2**	**4.2**	**2.0**	**2.2**	**2.5**	**1.1**	**1.3**	**1.4**
std (ms)	$\boldsymbol{NMPC_1}$	4.5	5.2	5.7	3.4	3.9	4.2	2.3	2.5	2.8	0.9	1.0	1.1	0.6	0.8	1.0
	$\boldsymbol{NMPC_2}$	**2.8**	**1.3**	**2.9**	**2.2**	**2.2**	**2.1**	**1.3**	**1.4**	**1.3**	**0.6**	**0.7**	**0.9**	**0.4**	**0.5**	**0.6**
max (ms)	$\boldsymbol{NMPC_1}$	57.0	64.1	65.3	36.7	40.0	42.9	15.0	16.8	18.7	6.4	7.2	8.2	4.0	4.7	5.3
	$\boldsymbol{NMPC_2}$	**28.1**	**25.9**	**28.1**	**19.1**	**18.9**	**18.9**	**8.6**	**8.9**	**8.8**	**4.4**	**4.9**	**5.9**	**2.5**	**3.1**	**3.4**

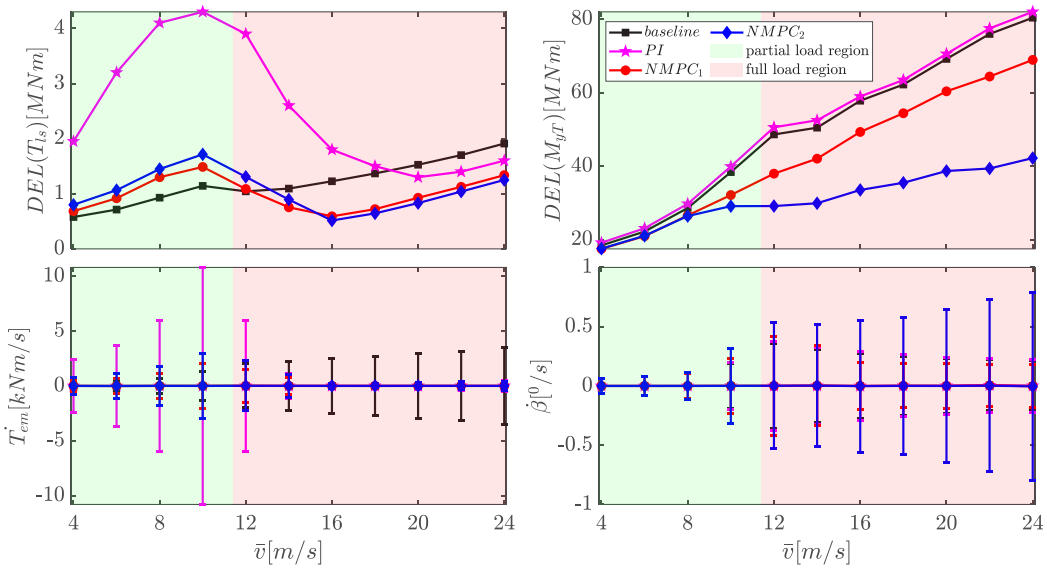

Fig. 9. Short-term damage-equivalent loads (DELs) on the shaft T_{ls} and tower M_{yT}, as well as statistical calculations for control input activity $\left(\dot{T}_{em} \text{ and } \dot{\beta}\right)$.

4- 1- 4- Statistical information and fatigue estimates

In this subsection, the MATLAB-based tool, MLife, calculates statistical information and estimates fatigue [40]. MLife was developed to post-process the data of WT experiments and dynamic, aeroelastic simulations. The statistical calculations cover minimum, mean, maximum, standard deviation, kurtosis, skewness, and maximum range. Damage rates and short-term damage-equivalent loads (DELs) based on a single time-series, lifetime DEL values based on the whole time-series data, and total lifetime damage and time to failure are part of the fatigue calculations. These calculations are made in this study using a Wöhler exponent of 4 [59], a design lifespan of 20 years, and a Rayleigh distribution ($C = 2\,m/s$).

Fig. 9 reports the statistical calculations to include the mean and standard deviation for the electromagnetic torque rate $\dot{T}_{em}$ and pitch angle rate $\dot{\beta}$, as well as the DELs for T_{ls} and M_{yT}. In $NMPC_1$ and $NMPC_2$ controllers, the tower's DEL is reduced not only for the full load region but also for the partial load region. The low-speed shaft's DEL and the electromagnetic torque activity $\dot{T}_{em}$ are only reduced for the full load region because the NMPC more accurately tracks the optimal TSR λ_{opt} in the partial load region. This causes a relatively more significant increase in power capture in the partial load region (see Table 5). The $NMPC_1$ controller's blade pitch activity, $\dot{\beta}$, decreases in the full load region but slightly increases in the partial load region, where a slight increase is useful for achieving optimization criteria. The $NMPC_2$ controller's blade pitch activity $\dot{\beta}$ is like that of the $NMPC_1$ controller in the partial-load region, but it increases in the full-load region. Accepting the cost of this increase will result in a considerable reduction in the tower's DEL.

Table 5 reports the aerodynamic η_{aero} and the electrical η_{elec} efficiency (Eq. (20)) for all wind bins. As can be seen, for NMPC controllers, both the aerodynamic η_{aero} and the electrical η_{elec} efficiency has been increased for all wind bins.

Table 6 summarizes the results for all 66 simulations. For $NMPC_1$, the possible lifetime DEL reduction of the low-speed shaft, the tower, and the out-of-plane blade root bending moment of blade 1 (Oop1) can be estimated at 11%, 12%, and 22%, respectively. Both the aerodynamic η_{aero} and the electrical η_{elec} efficiency has improved by an average of 1.7% and 1.4%, respectively. Furthermore, the standard deviation of the electromagnetic torque rate $\dot{T}_{em}$, pitch angle rate $\dot{\beta}$, generator power P_g, and generator speed ω_g decrease to approximately 60%, 0.3%, 32%, and 24% on average. Therefore, the $NMPC_1$ the controller can achieve all the control objectives specified in Section 2.3. However, in the case of the $NMPC_2$ controller, by reducing 39% of the standard deviations of the electromagnetic torque rate $\dot{T}_{em}$ and accepting a 14% increase in the shaft's lifetime DEL, this controller can improve both the aerodynamic η_{aero} and the electrical η_{elec} efficiency by 2% and 1.6%, respectively. This controller may also reduce the tower's lifetime DEL by

Table 5. Aerodynamic η_{aero} and the electrical η_{elec} efficiency for all wind bins.

	η_{aero}[%]				η_{elec}[%]			
$\bar{v}(m/s)$	$NMPC_1$	$NMPC_2$	$baseline$	PI	$NMPC_1$	$NMPC_2$	$baseline$	PI
4	98.2	**98.6**	97.6	82.4	93	**93**	93	75.9
6	98.5	**98.9**	98.1	84.5	93.5	**93.6**	93.5	79.2
8	98.4	**98.8**	97.8	83.2	93.1	93.1	**93.1**	78.1
10	94.2	**94.6**	93.5	79.8	**88.7**	88.6	88.6	72.4
12	73.6	**73.9**	70.5	58.4	69.6	**70.1**	66.7	51.6
14	49.6	**50.3**	46	36.8	47.1	**47.7**	43.5	32.4
16	33.8	**34.3**	30.6	27.9	32.1	**32.5**	29.1	25.1
18	23.9	**24.1**	21.6	18.9	22.7	**22.9**	20.5	18.7
20	17.3	**17.5**	15.7	13.8	16.5	**16.6**	14.9	14.8
22	12.9	**13.1**	11.8	10.9	12.3	**12.5**	11.2	11.3
24	9.9	**10.1**	9	8.7	9.5	**9.6**	8.6	8.9

Table 6. Overall improvement for the real-time NMPC with respect to the baseline controller.

Index [%] / Controller	$NMPC_1$	$NMPC_2$	Index [%] / Controller	$NMPC_1$	$NMPC_2$
Lifetime DEL (T_{ls})	**-10.9**	13.8	$\sigma(\dot{T}_{em})$	**-59.5**	-39.1
Lifetime DEL (M_{yT})	-12.4	**-39**	$\sigma(\dot{\beta})$	**-0.3**	82.1
Lifetime DEL (T_{Oop1})	**-22.3**	-22.2	$\sigma(P_g)$	-32.4	**-37.9**
η_{aero}	1.7	**2**	$\sigma(\omega_g)$	-24.3	**-46.8**
η_{elec}	1.4	**1.6**			

39% and the generator power and generator speed standard deviations by 38% and 47%, respectively, by accepting an 82% increase in the pitch angle rate standard deviation.

4- 2- Extreme loads

Different control techniques are compared in the time domain to see how they react to wind gusts. Consequently, extreme operation gusts at $v_{rated}+2m/s=13.2m/s$, and $v_{cut\_out}=25m/s$ are used to generate hub height time series according to standard [60]. Here, the NMPC, with the parameters described in Table 2, is compared to the baseline controller. Fig. 10 shows T_{em}, β, $\dot{T}_{em}$, $\dot{\beta}$, ω_g, ω_r, P_a, T_{ls}, and M_{yT} for three controllers and different wind speeds. In both simulations, the $NMPC_1$ controller, while having lower electromagnetic torque and blade pitch angle activity ($\dot{T}_{em}$ and $\dot{\beta}$) than the baseline and PI controllers, tries to reduce variations of ω_g, T_{ls}, and M_{yT}. With higher blade pitch angle activity than the baseline and PI controllers, the $NMPC_2$ controller may further reduce these variations.

4- 3- Presence of uncertainty

In this subsection, we repeat the simulations of Sections 4.1 and 4.2 for cases where complete and accurate wind speed information is not provided to the NMPC and when the model has uncertainties.

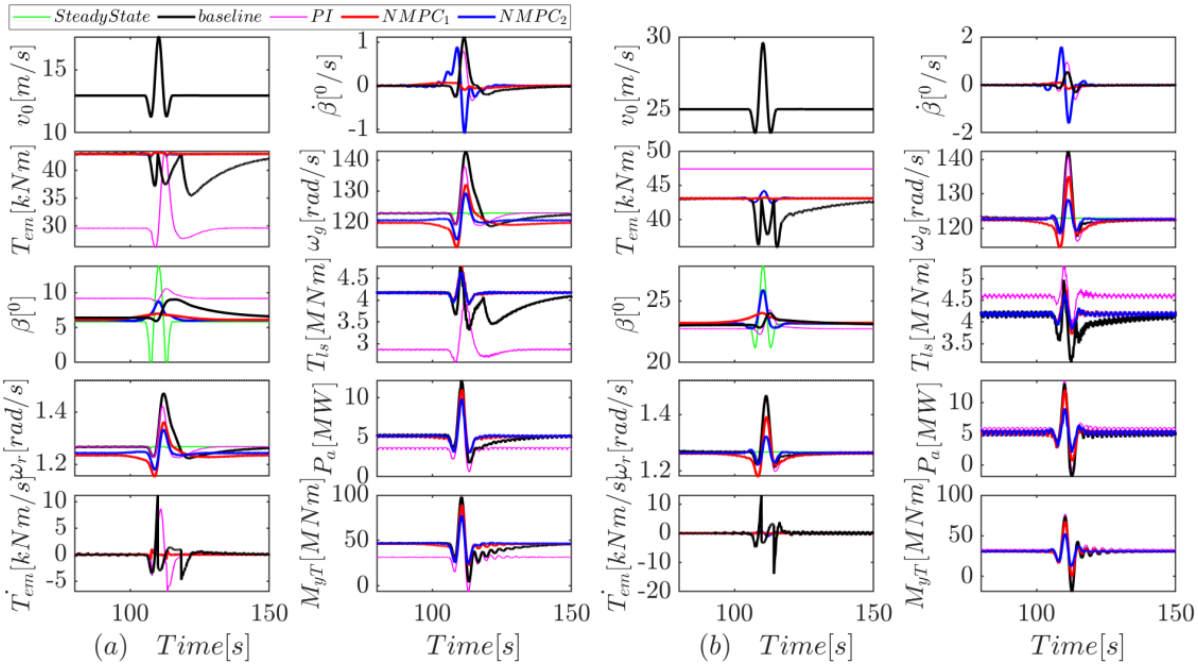

Fig. 10. Simulation results for extreme operation gusts at (a) v_0=13.2 m/s and (b) v_0=25 m/s.

4- 3- 1- Uncertainty in wind measurement

4-3-1-1- Limited LIDAR preview horizon

As demonstrated in Section 4.1.3, real-time NMPC deployment in the WTC with a relatively large NMPC horizon would be no problem. However, the limited LIDAR preview horizon may prevent us from doing so. Therefore, this section analyzes the loss in NMPC performance under the assumption of complete but limited LIDAR forecasts. Table 7 and Figs. 11 and 12 show this effect for the prediction horizons T =16.8,12,7.2,*and* 3.6s . As observed, the $NMPC_1$ performance is relatively weak for prediction horizons less than $T=12s$. So, it is better to choose a prediction horizon for $NMPC_1$ greater than $T=12s$. However, the performance of $NMPC_2$ is less sensitive to reducing the prediction horizon, and it may be decreased to $T=3.6s$.

4-4-1-2- Noisy wind speed

Furthermore, we evaluated the effect of wind speed measurement noise on NMPC efficiency, and the results are represented in Table 7 and Figs. 11 and 12. The standard deviation of wind speed noise is shown by σ in the figures. Because the classical tracking NMPC controller has inherently robust stability [61] and is also designed to avoid tracking high variations (see Section 3.1.1), wind speed measurement noise has little effect on NMPC performance.

4- 3- 2- Model uncertainty

In this section, we analyze the performance loss of the NMPC when the tower stiffness parameter, k_T , of the model is incorrect. $k_T{}^+=1.1k_T$ and $k_T{}^-=0.9k_T$ values are examined, producing a 5 percent uncertainty in the tower's fore-aft frequency. The simulation results demonstrate that the NMPC scheme is insensitive to modest k_T errors (see Table 7 and Figs. 11 and 12). This low sensitivity is attributed to the small discretization step size $\Delta\tau=0.1s$, allowing the NMPC to control uncertainty effectively.

5- Conclusion

In this paper, real-time NMPC is designed for the control of wind turbines (WT) over its all-operating regions. The controller has been implemented via two control loops that are connected with appropriate time constants. The inner loop includes the DFIG controller, and the outer loop contains the real-time NMPC controller. The NMPC is formulated using a parallel Newton-type method to be more efficient and implementable. The controller design is evaluated using a full aeroelastic model of the DFIG-based WT over the entire operating area with a set of standard wind profiles. The controller is comprehensively compared to a baseline controller. For NMPC, two sets of control parameters are established. The first set is modified to minimize stress loads on the blades, tower, and shaft and reduce control input

Table 7. Overall NMPC_1 performance in cases where the NMPC does not get complete and accurate wind speed information, as well as when the model includes uncertainties

Index [%]	uncertainty	$NMPC_1$	$NMPC_2$	Index [%]	uncertainty	$NMPC_1$	$NMPC_2$
Lifetime DEL (T_{ls})	$T = 21.6\ s$	-10.88	13.77	$\sigma(\dot{T}_{em})$	$T = 21.6\ s$	-59.54	-39.08
	$T = 16.8\ s$	-5.98	13.71		$T = 16.8\ s$	-59.31	-39.07
	$T = 12\ s$	-6.38	13.49		$T = 12\ s$	-59.20	-39.02
	$T = 7.2\ s$	-6.57	13.82		$T = 7.2\ s$	-57.21	-37.76
	$T = 3.6\ s$	-15.15	10.29		$T = 3.6\ s$	-65.94	-33.43
	K^+	-5.26	13.57		K^+	-59.76	-40.00
	k^-	-6.30	13.68		k^-	-59.12	-37.59
	$\sigma = 0.2$	-5.02	14.15		$\sigma = 0.2$	-59.06	-37.97
Lifetime DEL (M_{yT})	$T = 21.6\ s$	-12.37	-38.99	$\sigma(\dot{\beta})$	$T = 21.6\ s$	-0.28	82.10
	$T = 16.8\ s$	-13.65	-39.04		$T = 16.8\ s$	-0.05	82.84
	$T = 12\ s$	-13.13	-38.93		$T = 12\ s$	1.16	82.37
	$T = 7.2\ s$	-13.22	-38.20		$T = 7.2\ s$	10.41	82.51
	$T = 3.6\ s$	-12.24	-33.46		$T = 3.6\ s$	46.92	82.59
	K^+	-13.00	-38.09		K^+	-2.21	79.57
	k^-	-13.57	-39.13		k^-	1.33	89.05
	$\sigma = 0.2$	-13.67	-38.63		$\sigma = 0.2$	-1.99	83.89
Lifetime DEL (T_{oop1})	$T = 21.6\ s$	-22.34	-22.18	$\sigma(P_g)$	$T = 21.6\ s$	-32.37	-37.92
	$T = 16.8\ s$	-21.36	-22.25		$T = 16.8\ s$	-32.46	-37.92
	$T = 12\ s$	-21.25	-22.48		$T = 12\ s$	-32.54	-38.03
	$T = 7.2\ s$	-20.71	-22.55		$T = 7.2\ s$	-33.46	-37.98
	$T = 3.6\ s$	-22.06	-21.61		$T = 3.6\ s$	-40.72	-39.00
	K^+	-20.57	-20.91		K^+	-32.26	-37.67
	k^-	-21.50	-23.58		k^-	-32.53	-38.20
	$\sigma = 0.2$	-21.27	-22.14		$\sigma = 0.2$	-32.48	-37.85
η_{aero}	$T = 21.6\ s$	1.66	2.00	$\sigma(\omega_g)$	$T = 21.6\ s$	-24.22	-46.76
	$T = 16.8\ s$	1.37	1.76		$T = 16.8\ s$	-24.69	-46.77
	$T = 12\ s$	1.46	1.75		$T = 12\ s$	-25.00	-46.91
	$T = 7.2\ s$	1.59	1.75		$T = 7.2\ s$	-25.89	-46.86
	$T = 3.6\ s$	1.54	1.87		$T = 3.6\ s$	-30.11	-44.42
	K^+	1.47	1.80		K^+	-24.03	-46.20
	k^-	1.22	1.25		k^-	-24.55	-47.36
	$\sigma = 0.2$	1.36	1.56		$\sigma = 0.2$	-24.24	-46.64
η_{elec}	$T = 21.6\ s$	1.38	1.59				
	$T = 16.8\ s$	1.10	1.47				
	$T = 12\ s$	1.17	1.47				
	$T = 7.2\ s$	1.29	1.47				
	$T = 3.6\ s$	1.25	1.57				
	K^+	1.18	1.49				
	k^-	0.96	0.99				
	$\sigma = 0.2$	1.08	1.28				

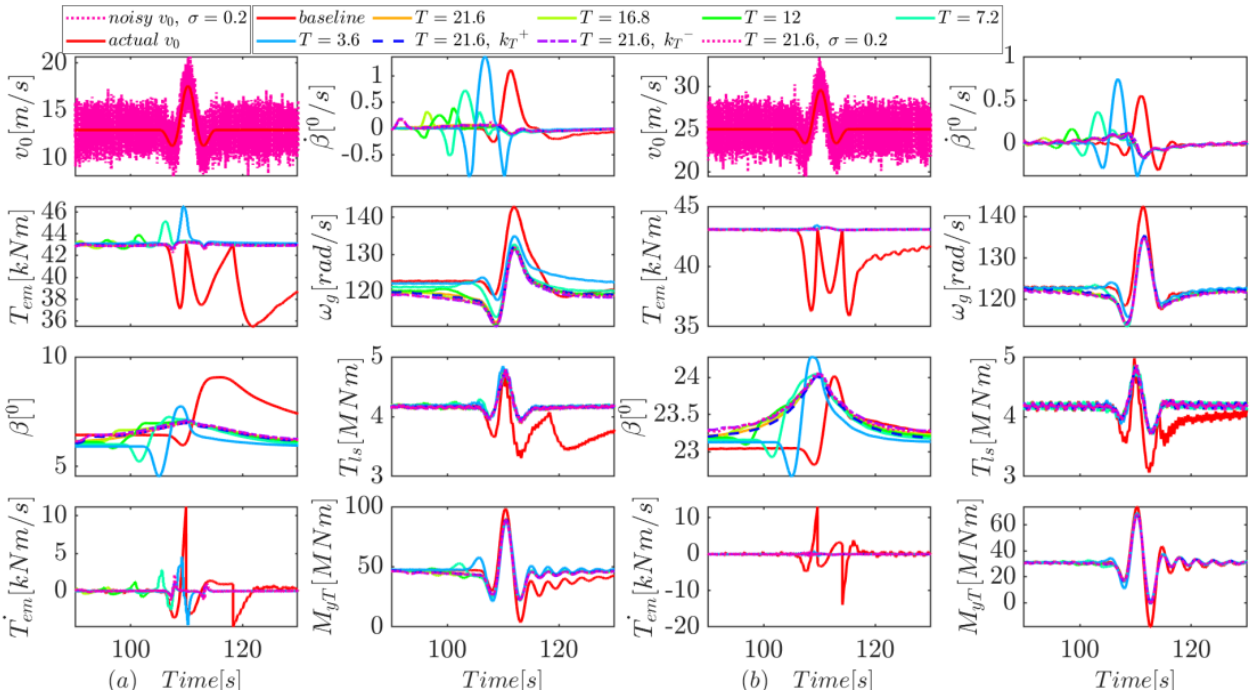

Fig. 11. NMPC$_1$ simulation results for extreme operation gusts at (a) v_0=13.2 m/s and (b) v_0=25 m/s in cases where the NMPC does not get complete and accurate wind speed information, as well as when the model includes uncertainties.

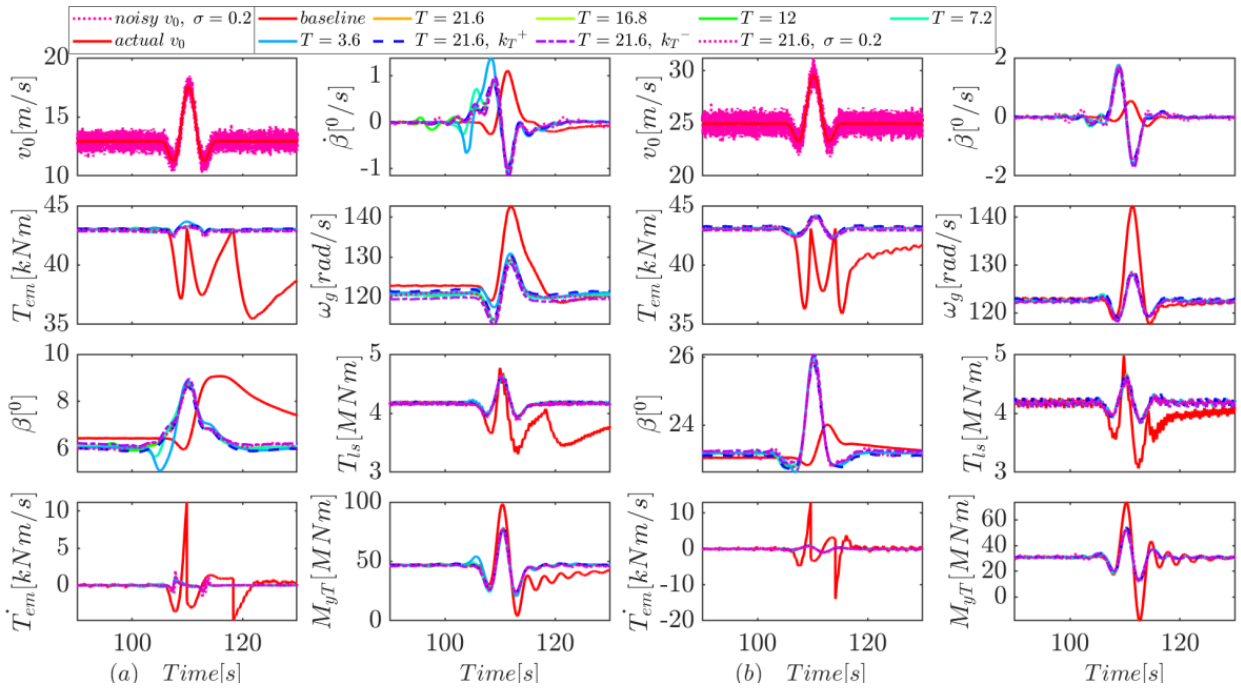

Fig. 12. NMPC$_2$ simulation results for extreme operation gusts at (a) v_0=13.2 m/s and (b) v_0=25 m/s in cases where the NMPC does not get complete and accurate wind speed information, as well as when the model includes uncertainties.

activity, increase power extraction, and smooth the generator's power and speed. In the second set, by accepting more pitch angle activity in the full load area and more generator torque activity in the partial load area, the fatigue load on the tower is further reduced, and more power is extracted from the wind. Computational time is also reduced. Furthermore, the NMPC scheme's robustness to an incorrect tower stiffness parameter, as well as its sensitivity to insufficient LIDAR prediction and the presence of measurement noise, have been evaluated.

The subject of future research is to design a predictive control strategy considering the economic aspects of WTs and the dynamic and stochastic aspects of wind speed. Furthermore, using a wind prediction provided by LIDAR and a wave prediction provided by buoys or SODAR, this strategy appears to be viable for controlling floating WTs.

Appendix

Appendix A: WT and DFIG parameters

See Tables A.1.

Table A.1. Specifications for the utilized aeroelastic WT [41] and DFIG model [25].

R	$63\ m$	$T_{em,rated}$	$43093.55\ Nm$
J_r	$387{,}592{,}28\ kg.m^2$	λ_{opt}	7.55
J_g	$534.116\ kg.m^2$	$C_{p_{opt}}$	0.482
K_r	$1972\ N.m.rad^{-1}.s^{-1}$	$\omega_{r,min}$	$0.722\ rad/s$
K_g	$4.235\ N.m.rad^{-1}.s^{-1}$	$\omega_{r,max}$	$1.1 \times 1.267\ rad/s$
K_{ls}	$6.215 \times 10^6\ N.m.rad^{-1}.s^{-1}$	$\omega_{g,min}$	$70.09\ rad/s$
B_{ls}	$8.67637 \times 10^8\ N.m.rad^{-1}$	$\omega_{g,max}$	$1.1 \times 122.9\ rad/s$
n_g	97: 1	$T_{em,max}$	$1.1 \times 43093.55\ Nm$
h_H	$90\ m$	β_{max}	$35\ deg$
m_T	$347{,}460\ kg$	$dT_{em,min}$	$-15000\ Nm$
m_N	$240{,}000\ kg$	$dT_{em,max}$	$15000\ Nm$
m_H	$56{,}780\ kg$	$d\beta_{min}$	$-8\ deg$
m_B	$17{,}740\ kg$	$d\beta_{max}$	$8\ deg$
f_0	$0.32\ Hz$	R_r	0.001446 Ω
d_s	0.01	R_s	0.001552 Ω
v_{cut-in}	$3\ m/s$	L_s	$0.0068\ H$
$v_{cut-out}$	$25\ m/s$	L_r	$0.0066\ H$
v_{rated}	$11.4\ m/s$	P	3
$\omega_{g,rated}$	$122.9\ rad/s$	M	$0.0055\ H$
$\omega_{g,cut-in}$	$70.09\ rad/s$		

Nomenclature

Variables

$C_P(\lambda,\beta)$	power coefficient
$C_q(\lambda,\beta)$	torque coefficient
$C_t(\lambda,\beta)$	thrust coefficient
F_a	thrust force, N
i_{rd}	direct axis rotor current, A
i_{rq}	quadrature axis rotor current, A
M_{yT}	tower base fore–aft bending moment, $N.m$
P_a	aerodynamic power, W
P_g	Generator power, W
T_a	aerodynamic torque, $N.m$
T_{em}	generator (electromagnetic) torque, $N.m$
T_{ls}	low speed shaft torque, $N.m$
T_{hs}	high speed shaft torque, $N.m$
v	effective wind speed, $m.s^{-1}$
v_0	natural wind speed, $m.s^{-1}$
v_{sd}	direct axis stator voltage, V
v_{sq}	quadrature axis stator voltage, V
v_{rd}	direct axis rotor voltage, V
v_{rq}	quadrature axis rotor voltage, V
x_T	tower top fore–aft displacement, m
β	pitch angle, deg
θ_r	rotor side angular deviation, rad
θ_g	generator side angular deviation, rad
θ_{ls}	gearbox side angular deviation, rad
θ_s	shaft torsion, rad
λ	tip speed ratio
ρ_{air}	air density, $kg.m^{-3}$
ρ	(d,q) reference frame position, rad
ϕ_{sd}	direct axis stator flux, Wb
ϕ_{sq}	quadrature axis stator flux, Wb
ω_r	rotor speed, $rad.s^{-1}$
ω_g	generator speed, $rad.s^{-1}$
ω_{ls}	low speed shaft speed, $rad.s^{-1}$
K_g	Generator external damping
K_{ls}	Low speed shaft damping
L_s	Stator inductance
L_r	Rotor inductance
M	Mutual inductance
m_B	Mass blade
m_T	Mass tower
m_N	Mass nacelle
m_H	Mass hub
n_g	Gearbox ration
P	Number of pole pairs
R	Rotor radius
R_r	Rotor resistance
R_s	Stator resistance
$T_{em,max}$	Maximum electromagnetic torque
$T_{em,rated}$	Rated electromagnetic torque
v_{cut-in}	Cut-in Wind Speed
$v_{cut-out}$	Cut-out wind speed
v_{rated}	Rated wind speed
β_{max}	Maximum blade pitch angle
λ_{opt}	Optimal tip speed ratio
$\omega_{g,rated}$	Rated generator speed
$\omega_{g,cut-in}$	Cut-in generator speed
$\omega_{r,min}$	Minimum rotor speed
$\omega_{r,max}$	Maximum rotor speed
$\omega_{g,min}$	Minimum generator speed
$\omega_{g,max}$	Maximum generator speed

Abbreviations

ADAMS	Automatic dynamic analysis of mechanical system
CPC	Collective pitch control
DEL	Damage-equivalent load
DFIG	Doubly fed induction generator
FAST	Fatigue, aerodynamics, structure, and turbulence

	Parameters
B_{ls}	Low speed shaft stiffness
$C_{p_{opt}}$	Optimal power coefficient
$dT_{em,min}$	Minimum electromagnetic torque rate
$dT_{em,max}$	Maximum electromagnetic torque rate
$d\beta_{min}$	Minimum blade pitch angle rate
$d\beta_{max}$	Maximum blade pitch angle rate
d_s	Structural damping ratio
f_0	Natural frequency of first tower fore–aft bending
h_H	Hub height
J_r	Rotor inertia
J_g	Generator inertia
K_r	Rotor external damping

FHOCP	Finite horizon optimal control problem
FPGA	Field programmable gate array
LIDAR	Light detection and ranging
MIMO	Multiple-input multiple-output
MPC	Model predictive control
MPPT	Maximum power point tracking
NLP	Nonlinear programming problem
NMPC	Nonlinear model predictive control
NREL	National renewable energy laboratory
OCP	Optimal control problem
TSR	Tip speed ratio
VSWT	Variable speed wind turbine
WT	Wind turbine
WTC	Wind turbine control

References

[1] B. Amoco, Statistical review of world energy. [London],[BP Amoco Plc], in, 2018.

[2] O. Anaya-Lara, N. Jenkins, J.B. Ekanayake, P. Cartwright, M. Hughes, Wind energy generation: modelling and control, John Wiley & Sons, 2011.

[3] I. Munteanu, A.I. Bratcu, E. CeangĂ, N.-A. Cutululis, Optimal control of wind energy systems: towards a global approach, Springer, 2008.

[4] A. Kusiak, Z. Zhang, A. Verma, Prediction, operations, and condition monitoring in wind energy, energy, 60 (2013) 1-12.

[5] E. Bossanyi, Wind turbine control for load reduction, Wind Energy: An International Journal for Progress and Applications in Wind Power Conversion Technology, 6(3) (2003) 229-244.

[6] S. Wang, Y. Xing, A. Karuvathil, O. Gaidai, A comparison study of power performance and extreme load effects of large 10-MW offshore wind turbines, IET Renewable Power Generation, (2023).

[7] I.P. Girsang, J.S. Dhupia, E. Muljadi, M. Singh, L.Y. Pao, Gearbox and drivetrain models to study dynamic effects of modern wind turbines, IEEE Transactions on Industry Applications, 50(6) (2014) 3777-3786.

[8] J.G. Njiri, D. Söffker, State-of-the-art in wind turbine control: Trends and challenges, Renewable and Sustainable Energy Reviews, 60 (2016) 377-393.

[9] M. Harris, M. Hand, A. Wright, Lidar for turbine control, National Renewable Energy Laboratory, Golden, CO, Report No. NREL/TP-500-39154, (2006).

[10] M. Sawant, S. Thakare, A.P. Rao, A.E. Feijóo-Lorenzo, N.D. Bokde, A review on state-of-the-art reviews in wind-turbine-and wind-farm-related topics, Energies, 14(8) (2021) 2041.

[11] C. Pavese, Wind energy literature survey no. 34, Wind Energy, 18(7) (2015) 1313-1316.

[12] M.A. Hannan, A.Q. Al-Shetwi, M.S. Mollik, P.J. Ker, M. Mannan, M. Mansor, H.M.K. Al-Masri, T.M.I. Mahlia, Wind Energy Conversions, Controls, and Applications: A Review for Sustainable Technologies and Directions, Sustainability, 15(5) (2023) 3986.

[13] M.G.M. Almihat, M.T. Kahn, Wind Turbines Control Trends and Challenges: An Overview, International Journal of Innovative Research and Scientific Studies, 5(4) (2022) 378-390.

[14] M.E.B. Aguilar, D.V. Coury, R. Reginatto, R.M. Monaro, Multi-objective PSO applied to PI control of DFIG wind turbine under electrical fault conditions, Electric Power Systems Research, 180 (2020) 106081.

[15] S.-h. Hur, W.E. Leithead, Model predictive and linear quadratic Gaussian control of a wind turbine, Optimal Control Applications and Methods, 38(1) (2017) 88-111.

[16] R.F. Nayeh, H. Moradi, G. Vossoughi, Multivariable robust control of a horizontal wind turbine under various operating modes and uncertainties: A comparison on sliding mode and H∞ control, International Journal of Electrical Power & Energy Systems, 115 (2020) 105474.

[17] G. Rigatos, P. Siano, M. Abbaszadeh, P. Wira, Nonlinear optimal control for wind power generators comprising a multi-mass drivetrain and a DFIG, Journal of the Franklin Institute, 356(5) (2019) 2582-2605.

[18] K.A. Naik, C.P. Gupta, E. Fernandez, Design and implementation of interval type-2 fuzzy logic-PI based adaptive controller for DFIG based wind energy system, International Journal of Electrical Power & Energy Systems, 115 (2020) 105468.

[19] F.D. Bianchi, R.S. Sánchez-Peña, M. Guadayol, Gain scheduled control based on high fidelity local wind turbine models, Renewable energy, 37(1) (2012) 233-240.

[20] A. Wu, B. Zhao, J. Mao, B. Wu, F. Yu, Adaptive active fault-tolerant MPPT control for wind power generation system under partial loss of actuator effectiveness, International Journal of Electrical Power & Energy Systems, 105 (2019) 660-670.

[21] A.D. Bebars, A.A. Eladl, G.M. Abdulsalam, E.A. Badran, Internal electrical fault detection techniques in DFIG-based wind turbines: A review, Protection and Control of Modern Power Systems, 7(1) (2022) 18.

[22] C. Evangelista, F. Valenciaga, P. Puleston, Active and reactive power control for wind turbine based on a MIMO 2-sliding mode algorithm with variable gains, IEEE Transactions on Energy Conversion, 28(3) (2013) 682-689.

[23] L. Xiong, P. Li, F. Wu, M. Ma, M.W. Khan, J. Wang, A coordinated high-order sliding mode control of DFIG wind turbine for power optimization and grid synchronization, International Journal of Electrical Power & Energy Systems, 105 (2019) 679-689.

[24] Y. Mousavi, G. Bevan, I.B. Kucukdemiral, A. Fekih, Sliding mode control of wind energy conversion systems: Trends and applications, Renewable and Sustainable Energy Reviews, 167 (2022) 112734.

[25] A. Bektache, B. Boukhezzar, Nonlinear predictive control of a DFIG-based wind turbine for power capture optimization, International journal of electrical power & Energy systems, 101 (2018) 92-102.

[26] M. Soliman, O. Malik, D. Westwick, Multiple model MIMO predictive control for variable speed variable pitch wind turbines, in: Proceedings of the 2010 American Control Conference, IEEE, 2010, pp. 2778-2784.

[27] P. Jiang, T. Zhang, J. Geng, P. Wang, L. Fu, An MPPT Strategy for Wind Turbines Combining Feedback Linearization and Model Predictive Control, Energies, 16(10) (2023) 4244.

[28] P.P. Pradhan, B. Subudhi, A. Ghosh, A new optimal model predictive control scheme for a wind energy conversion system, International Journal of Numerical Modelling: Electronic Networks, Devices and Fields, 35(3) (2022) e2976.

[29] Y. Hu, T.K. Chau, X. Zhang, H.H.-C. Iu, T. Fernando, D. Fan, A Novel Adaptive Model Predictive Control Strategy for DFIG Wind Turbine with Parameter Variations in Complex Power Systems, IEEE Transactions on Power Systems, (2022).

[30] A. Koerber, R. King, Nonlinear model predictive control for wind turbines, Proc. EWEA, (2011).

[31] D. Schlipf, D.J. Schlipf, M. Kühn, Nonlinear model predictive control of wind turbines using LIDAR, Wind energy, 16(7) (2013) 1107-1129.

[32] W.R. Sultana, S.K. Sahoo, S. Sukchai, S. Yamuna, D. Venkatesh, A review on state of art development of model predictive control for renewable energy applications, Renewable and sustainable energy reviews, 76 (2017) 391-406.

[33] W.H. Lio, J. Rossiter, B.L. Jones, A review on applications of model predictive control to wind turbines, in: 2014 Ukacc international conference on control (control), IEEE, 2014, pp. 673-678.

[34] D. Song, J. Yang, M. Dong, Y.H. Joo, Model predictive control with finite control set for variable-speed wind turbines, Energy, 126 (2017) 564-572.

[35] M. Darabian, A. Jalilvand, Predictive control strategy to improve stability of DFIG-based wind generation connected to a large-scale power system, International Transactions on Electrical Energy Systems, 27(5) (2017) e2300.

[36] O. Von Stryk, R. Bulirsch, Direct and indirect methods for trajectory optimization, Annals of operations research, 37 (1992) 357-373.

[37] V. Boltyanskiy, R.V. Gamkrelidze, Y. Mishchenko, L. Pontryagin, Mathematical theory of optimal processes, (1962).

[38] H. Deng, T. Ohtsuka, A parallel Newton-type method for nonlinear model predictive control, Automatica, 109 (2019) 108560.

[39] S. Gros, M. Vukov, M. Diehl, A real-time MHE and NMPC scheme for wind turbine control, in: 52nd IEEE Conference on Decision and Control, IEEE, 2013, pp. 1007-1012.

[40] G. Hayman, MLife theory manual for version 1.00, National Renewable Energy Laboratory, Golden, CO, 74(75) (2012) 106.

[41] J. Jonkman, S. Butterfield, W. Musial, G. Scott, Definition of a 5-MW reference wind turbine for offshore system development, National Renewable Energy Lab. (NREL), Golden, CO (United States), 2009.

[42] B. Jonkman, Turbsim user's guide v2. 00.00, Natl. Renew. Energy Lab, (2014).

[43] S. Heier, Grid integration of wind energy: onshore and offshore conversion systems, John Wiley & Sons, 2014.

[44] ADAMS: The multibody dynamic simulation solution, in, 2015.

[45] J. Jonkman, M.L. Buhl Jr, NWTC information portal (FAST), National Renewable Energy Laboratory, Golden, CO, accessed May, 11 (2015) 2016.

[46] G.H. Bladed: A design tool for wind turbine performance and loading, in, 2015.

[47] S. Øye, FLEX5 Simulation Software, DTU Wind Energy.

[48] B. Boukhezzar, H. Siguerdidjane, Nonlinear control of a variable-speed wind turbine using a two-mass model, IEEE transactions on energy conversion, 26(1) (2010)

149-162.

[49] M.A. Abdelbaky, X. Liu, D. Jiang, Design and implementation of partial offline fuzzy model-predictive pitch controller for large-scale wind-turbines, Renewable Energy, 145 (2020) 981-996.

[50] S.-h. Hur, Modelling and control of a wind turbine and farm, Energy, 156 (2018) 360-370.

[51] J. Björnstedt, Integration of non-synchronous generation-frequency dynamics, Lund University, 2012.

[52] W. Srirattanawichaikul, S. Premrudeepreechacharn, Y. Kumsuwan, A comparative study of vector control strategies for rotor-side converter of DFIG wind energy systems, in: 2016 13th International Conference on Electrical Engineering/Electronics, Computer, Telecommunications and Information Technology (ECTI-CON), IEEE, 2016, pp. 1-6.

[53] R. Marino, P. Tomei, C.M. Verrelli, Induction motor control design, Springer Science & Business Media, 2010.

[54] E.A. Bossanyi, The design of closed loop controllers for wind turbines, Wind energy: An International Journal for Progress and Applications in Wind Power Conversion Technology, 3(3) (2000) 149-163.

[55] J.M. Maciejowski, in: Predictive Control with Constraints, Prentice Hall, 2000.

[56] R.H. Byrd, M.E. Hribar, J. Nocedal, An interior point algorithm for large-scale nonlinear programming, SIAM Journal on Optimization, 9(4) (1999) 877-900.

[57] S.V. Rakovic, W.S. Levine, Handbook of model predictive control, Springer, 2018.

[58] T. Faulwasser, Optimization-based solutions to constrained trajectory-tracking and path-following problems, Magdeburg, Universität, Diss., 2012, 2013.

[59] E. Bossanyi, B. Savini, M. Iribas, M. Hau, B. Fischer, D. Schlipf, T. van Engelen, M. Rossetti, C. Carcangiu, Advanced controller research for multi-MW wind turbines in the UPWIND project, Wind Energy, 15(1) (2012) 119-145.

[60] W. Turbines, Part 1: Design Requirements, IEC 61400-1, International Electrotechnical Commission: Geneva, Switzerland, (2005).

[61] C.M. Kellett, A.R. Teel, Smooth Lyapunov functions and robustness of stability for difference inclusions, Systems & Control Letters, 52(5) (2004) 395-405.

HOW TO CITE THIS ARTICLE

M. Soleymani, M. Rahmani, N. Bigdeli, Parallel Real-time Nonlinear Model Predictive Control of DFIG-based Wind Turbines over All Operating Regions, AUT J. Elec. Eng., 55(3) (Special Issue) (2023) 417-440.

DOI: 10.22060/eej.2023.22276.5528